Electrochimica Acta 439 (2023) 141583

Contents lists available at ScienceDirect

Electrochimica Acta

journal homepage: www.journals.elsevier.com/electrochimica-acta

Internally-externally molecules-scissored ramie carbon for high performance electric double layer supercapacitors

Yuyang Chen [a], Qing Wang [a], Ningjun Chen [a], Qitian Luo [a], Haijian Li [b], Jie Li [b], Weiqing Yang [a,b,*]

[a] Key Laboratory of Advanced Technologies of Materials, Ministry of Education, School of Materials Science and Engineering, Southwest Jiaotong University, Chengdu 610031, China

[b] Jinshi Technology Co. Ltd., 289 Longquanyi District, Chengdu 610100, China

ARTICLE INFO

Keywords:
Ramie straw biomass
Internally-externally molecules-scissored activation
Supercapacitors
Cyclic stability
Waste utilization

ABSTRACT

Ramie carbon from the massively three-harvests-one-year and naturally channel-structured ramie straw is typically emerging as the excellent waste-biomass-utilization target toward high-performance electrochemical energy storage devices. However, the traditional activation strategies less fully optimize the pore distribution for the purpose of optimal energy storage capability. Herein, we reported the hierarchically interconnected three-dimensional ramie porous carbon based on waste ramie straw by internally-externally molecules-scissored activation strategy with pre-embedded KOH and re-added KOH molecules coordinately (in-ex-RPC). Benefiting from the synergistically internal-external activation strategy, this in-ex-RPC displays an excellent specific capacitance of 300 F g^{-1}, which is much better than that of ramie porous carbon singly through pre-embedded KOH activation (in-RPC, 194 F g^{-1}) or directly adding KOH activation (ex-RPC, 213 F g^{-1}). Based on it, the aqueous symmetric supercapacitors display a cyclic capacity of 90.9%-retaining after 20,000 cycles at 5 A g^{-1}. Therefore, this work may provide an effective strategy for energy storage applications of waste ramie straw and for further promoting waste biomass utilization.

1. Introduction

Recycling the waste biomass, such as ramie straw, corn straw, wheat stalk et.al, could fully excavate potential utilization value and usefully bring into playing a significant role in sustainable development [1]. Typically, the waste biomass is transformed into biomass carbon by utilizing corrosive chemical reagents, such as potassium hydroxide (KOH), phosphoric acid (H_3PO_4), zinc chloride ($ZnCl_2$), potassium carbonate (K_2CO_3), or making use of steam and carbon dioxide (CO_2) toward the strongly demanding electrochemical energy storage devices, such as lithium-ion batteries [2–7], lithium-sulfur batteries [8–11] and supercapacitors [12–20]. Especially, the ever-increasing supercapacitors have currently cried for the high-quality biomass carbon which possesses excellent pore distribution including large porosity and high specific surface area. Therefore, it is necessary to choose appropriate activation strategies to enhance porosity and specific surface area and to further acquire excellent pore distribution.

In this regard, the traditional activation strategies, including physical activation strategies such as microwave heating [21,22], steam activation [23,24], CO_2 activation [25–27], and chemical activation strategies such as KOH activation [28–31], H_3PO_4 activation [32,33], $ZnCl_2$ activation [15,34] and K_2CO_3 activation [35–37], are wholly used to successfully prepare the hierarchical-pore biomass carbon for supercapacitors. Although these traditional activation strategies could achieve the good quality biomass carbon, it is difficult to satisfy the extremely harsh quality of high-performance biomass carbon based supercapacitors.

In this work, the massively three-harvests-one-year and naturally channel-structured ramie straw is employed to construct the hierarchically interconnected three-dimensional porous carbon through the internally-externally molecules-scissored activation with pre-embedded KOH and re-added KOH molecules coordinately (This carbon can be simply named as in-ex-RPC). This as-prepared in-ex-RPC with a high specific surface area of 1656 m^2 g^{-1}, high pore volume of 2.74 cm^3 g^{-1} and average pore diameter of 6.48 nm displays a specific capacitance of 300 F g^{-1}, which is much better than that of ramie porous carbon singly

* Corresponding author.
E-mail address: wqyang@swjtu.edu.cn (W. Yang).

https://doi.org/10.1016/j.electacta.2022.141583
Received 4 September 2022; Received in revised form 18 October 2022; Accepted 20 November 2022
Available online 21 November 2022

through pre-embedded KOH activation (in-RPC, 194 F g^{-1}) or directly adding KOH activation (ex-RPC, 213 F g^{-1}). Based on it, the aqueous 6 M KOH based symmetric supercapacitors deliver a high energy density of 9.125 W h kg^{-1}, a high power density of 0.5 kW kg^{-1} and a cyclic capacity of 90.9%-retaining after 20,000 cycles at 5 A g^{-1}. Simultaneously, the 1-ethyl-3-methyl imidazolium tetrafluoroborate salt ($EMIMBF_4$) ionic liquid electrolyte based symmetric supercapacitors supply a high energy density of 65.5 W h kg^{-1} and a high power density of 1.76 KW kg^{-1}. Therefore, we believed that this internally-externally molecules-scissored activation strategy should contribute to energy storage applications of waste ramie straw and further promote clean utilization of waste biomass.

2. Experimental section

2.1. Materials

Ramie straw (DaZhou, SiChuan), potassium hydroxide (chron chemicals, ChengDu), Polytetrafluoroethylene (aladdin, ShangHai), hydrochloric acid, superC45, commercial activated carbon (YP-50F), isopropyl alcohol (aladdin, ShangHai), nickel foam, $EMIMBF_4$ ionic liquid (macklin, ShangHai), cellulose membrane. All solutions were prepared by using ultrapure water.

2.2. Synthesis of ramie straw-derived precursor

First, ramie straw was pulverized and dispersed 1.5 g into 3 M KOH solution at 30 ml. Then, the mixture was transferred into high pressure reactors at 50 ml and heated to 180 °C and stayed at 6 h in the oven. Finally, the treated mixture was filtered to remove impurities (hemicellulose and lignin) when naturally cooled to room temperature. Finally, the obtained precursor was dried for 12 h in the oven.

2.3. Synthesis of ramie straw-derived porous carbon (in-ex-RPCs)

First of all, the precursor and Polytetrafluoroethylene (PTFE, 60 wt% dispersion in water) were weighed based on the weight ratio of them with 1:1. Then, sheet potassium hydroxide (KOH) was weighed based on the weight ratio of KOH to precursor and PTFE (from 1:1 to 6:1), and mixed with 5 ml ultrapure water under magnetic stirred for 20 min at room temperature. After that, the mixtures were further agitated for several time in an oil bath at 80 °C to obtain thick mixture. Afterwards, the thick mixtures were transferred into a porcelain boat and dried for 3 h in the oven. And the dried samples were transferred into a tube furnace and firstly kept constant at 450 °C for 1 h and followed by reacted at 700 °C for 1 h under Ar atmosphere with gas flow at 40 sccm. Finally, waiting for the tube furnace to cool naturally and taking out the samples and using 1 M hydrochloric acid (HCl) for at least 8 h to remove residual KOH. Later, the samples were rinsed repeatedly with ultrapure water until pH reached at 7 and dried out for 12 h at 120 °C in the oven. the obtained samples were denoted as in-ex-RPC. The samples only through the pre-embedded KOH or directly adding KOH activation were prepared by the above method and denoted as in-RPC and ex-RPC, respectively.

2.4. Sample characterizations

The chemical compositions (cellulose, hemicellulose, lignin and ash content) of the ramie straw were measured by cellulose analyzer (CA, FIWE Advance, Italy). The microstructures of samples were characterized by scanning electron microscopy (SEM) (JEOL JSM-7800 Prime) and transmission electron microscopy (TEM) (JEOL JEM-2100F) respectively. X-ray diffraction (XRD) patterns were acquired the phases on a PANalytical X'Pert powder diffractometer with Cu Kα source and 2θ ranges from 15° to 60° Raman spectra measurements were recorded by a RM 2000 microscopic confocal Raman spectrometer with a 532 nm laser beam to determine the defects state of carbon materials. Energy dispersive X-ray spectrometer (EDS) (JEOL JSM-7800 Prime) and X-ray photoelectron spectroscopy (XPS) patterns were conducted on a Thermo Scientific™ K-Alpha™$^+$ spectrometer equipped with a monochromatic Al Kα X-ray source (1486.6 eV) operating at 100 W to confirm the basic composition. The Brunauer-Emmett-Teller (BET) surface area and density functional theory (DFT) pore size distribution of carbon materials were measured by Micromeritics ASAP 2460 specific surface area and pore size analyzer through N_2 adsorption/desorption isotherm at 77 K, and before BET test, outgassing the samples at 200 °C for 2 h to make the pores be fully exposed. The Fourier transform infrared spectroscopy (FTIR) patterns were obtained to determine the types and changes of functional groups from the carbon materials using a TENSOR II spectrometer (Bruker).

2.5. Electrochemical measurements

The electrode materials of supercapacitors were prepared by ramie porous carbon (RPCs) and activated carbon (AC), superC45 and 10 wt% PTFE with a mass ratio of 8:1:1 mixed with isopropyl alcohol. The mixtures were placed in an oven at 85 °C to remove excess isopropyl alcohol after blended for at least 10 min. Then, the mixtures were rolled to 80 um thick slice and punch into wafer-shaped electrodes with a diameter of 10 mm. And then, the wafer-shaped electrodes and nickel foams were compressed to combine, and a cellulose membrane was sandwiched into two RPCs and AC electrodes that fully wetted with 6 M KOH solution or $EMIMBF_4$ ionic liquid for the CR2032 coin-type cells. Finally, the cyclic voltammetry curves (CV), galvanostatic charge/discharge curves (GCD) and electrochemical impedance spectroscopy curves (EIS) were conducted with a CHI660E electrochemical workstation (Chenhua, Shanghai, China), and the cycling stability was carried out on Neware measurement system.

3. Results and discussions

Fig. 1 schematically demonstrates the internally-externally molecules-scissored activation process and microstructure images of ramie porous carbon. As shown in Fig. 1a and S2a-b, the ramie porous carbon is constructed through the pre-embedded KOH and re-added KOH molecules activation (in-ex-RPC), the pre-embedded KOH activation (in-RPC) or directly added KOH molecules activation (ex-RPC) originated from the naturally channel-structured ramie straw (Fig. S1 and Table S1). Specifically speaking, the vacancy defects are produced by the reaction of carbon substrate and KOH molecules. In Fig. 1b-d, all the in-ex-RPC, in-RPC and ex-RPC almost perform the porous structures towards energy storage capability of supercapacitors. Compared with ex-RPC or in-RPC, in-ex-RPC can present more mesopores and macropores, which are beneficial for charge transmission.

Fig. 2 displays the microstructures of in-ex-RPC in detail. In Fig. 2a-b, in-ex-RPC obviously demonstrates the abundant interconnected porous structures through the pre-embedded KOH and re-added KOH molecules activation cooperatively. And in Fig. 2c-d and S3a-f, TEM images of in-ex-RPC, in-RPC and ex-RPC can apparently perform porous structures. Also, the high magnification TEM images display abundant mesopores and micropores structures. Then, the EDS images shows the carbon (C) element weight ratio of up to 94.8% (Fig. 2e-i and Table S2), while the total weight ratios of potassium (K) and chlorine (Cl) elements are lower than 1%, and no fluorine (F) element exists, revealing the high carbon content after carbonization. This optimal porous distribution can provide the substantial ions interacted active sites and sufficient 3D-interconnected channels, guaranteeing charge-reserved accommodation and rapidly charge-transferred paths for high-performance supercapacitors.

Further, Fig. 3 shows the crystal structure and surface characteristics of in-ex-RPC, in-RPC and ex-RPC. In Fig. 3a, X-ray patterns of all the in-ex-RPC, in-RPC and ex-RPC exhibit two broad peaks at 23° and 43°,

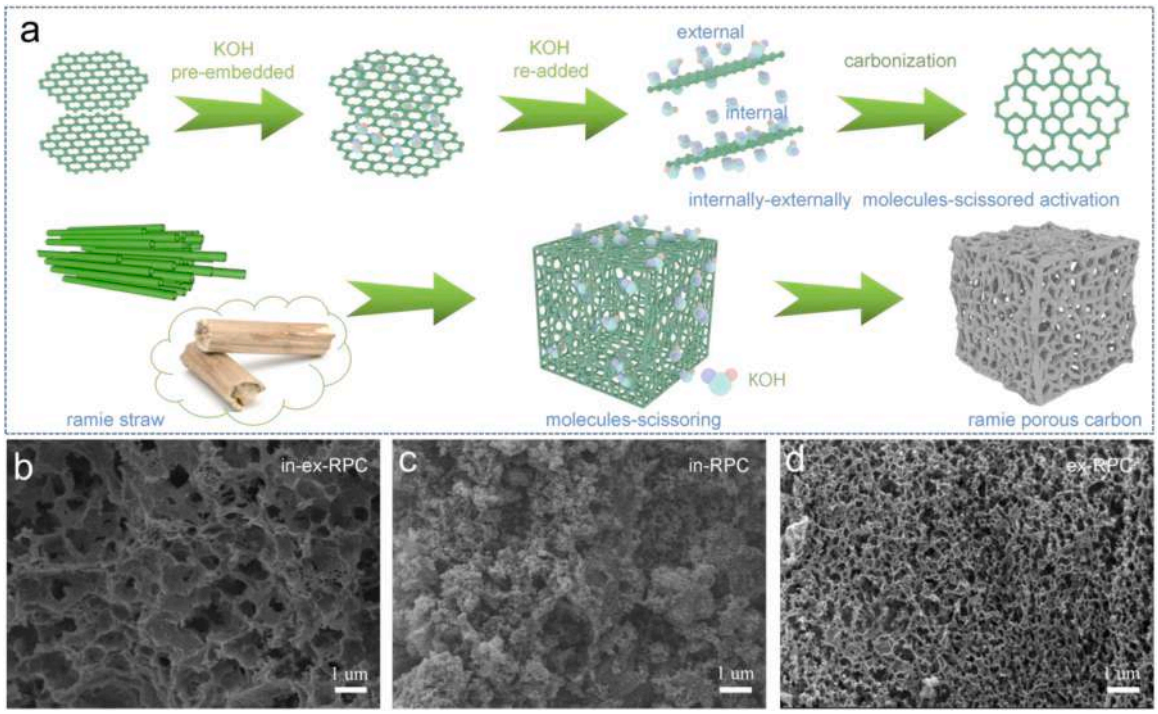

Fig. 1. The schematic internally-externally molecules-scissored activation process and microstructure images of ramie porous carbon. (a) Activation process of in-ex-RPC. (b-d) SEM images of in-ex-RPC, in-RPC and ex-RPC, respectively.

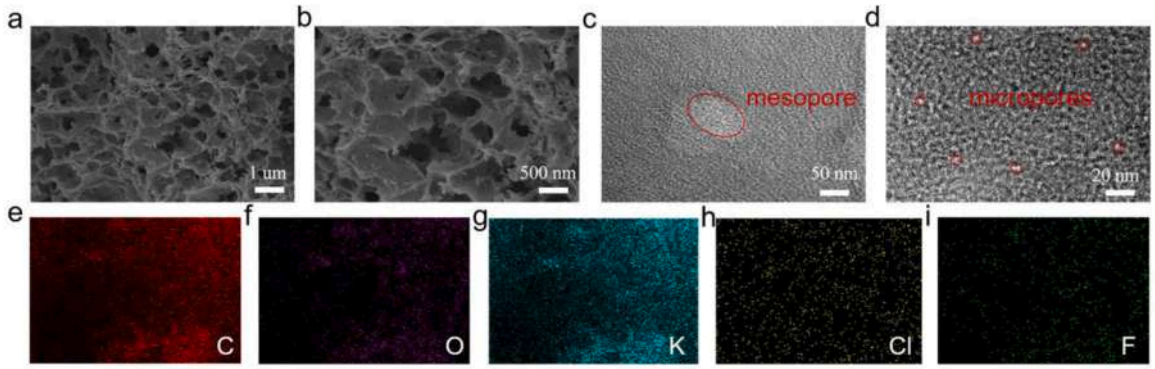

Fig. 2. The microstructures of ramie porous carbon (in-ex-RPC). (a-b) SEM images of in-ex-RPC at different magnifications. (c-d) TEM images of in-ex-RPC at high magnification with abundant mesopore and micropore structures. (e-i) Elemental mapping images for C, O, K, Cl and F elements of in-ex-RPC, respectively.

while the weaker and broader (002) peak of in-ex-RPC than those of in-RPC and ex-RPC obviously illustrates more carbon disordered structures [38,39]. Simultaneously, the Raman spectra of in-ex-RPC, in-RPC and ex-RPC display two characteristic peaks at 1358 cm^{-1} and 1588 cm^{-1}, corresponding to *D*-band (disordered carbon) and *G*-band (ordered graphite carbon), respectively. Their intensity ratio I_D/I_G are fitted to be 2.08, 1.33 and 1.53, respectively (Fig. 3b). The higher ratio of in-ex-RPC reveals the more disordered structures properties, which is well consistent with the result of XRD patterns.

Besides, in Fig. 3c, three Fourier transform infrared spectroscopy (FTIR) spectra display the adsorption band which represents the stretching vibration of -OH from the carbon surface at about 3440 cm^{-1}. Also, the adsorption bands of C—H symmetric and asymmetric stretching of CH_2 and CH_3 groups are at about 2800–3000 cm^{-1}, and the adsorption band at approximately 1730 cm^{-1} corresponds to the in-plane bending vibration of C = O. Then, the adsorption band at about 1630 cm^{-1}, referring to the skeleton vibration of aromatic C = C. Finally, these bands are probably related to the C—O stretching vibration at approximately 1269 cm^{-1} and 1000–1200 cm^{-1} [40,41]. The more asymmetric stretching of CH_2, CH_3 groups and C = C groups from in-ex-RPC than those of in-RPC and ex-RPC illustrates the existence of more disordered structures, and also the more C = O and C—O groups from in-ex-RPC reveals the higher unsaturation degree to form more active sites. In Fig. S4 and 3d, all the X-ray photoelectron spectroscopy (XPS) full-scan spectra show the presence of carbon (C) and oxygen (O) element in the three samples. The whole C 1 s spectra can be deconvolved into four components at 284.8 eV, 286.3 eV, 287.7 eV and 288.7 eV, which are attributed to C—C/C = C, C—O, C = O and O—C = O, respectively. And the deconvolution of the O1s XPS spectra yields two peaks at 531.7 eV and 533.0 eV, which are attributed to double-bounded O atoms in esters, carbonates and acids, as well as to single bounded O atoms in ketons, ethers and alcohols, indicating that oxygen basically occurs in the form of functional groups and there are no oxygen vacancies onto in-ex-RPC sample. [40] Meanwhile, the Table 1 shows the atomic ratio of oxygen element slightly reduces from 95.1% (ex-RPC) to 93.3% (in-ex-RPC), indicating that oxygen-containing groups are

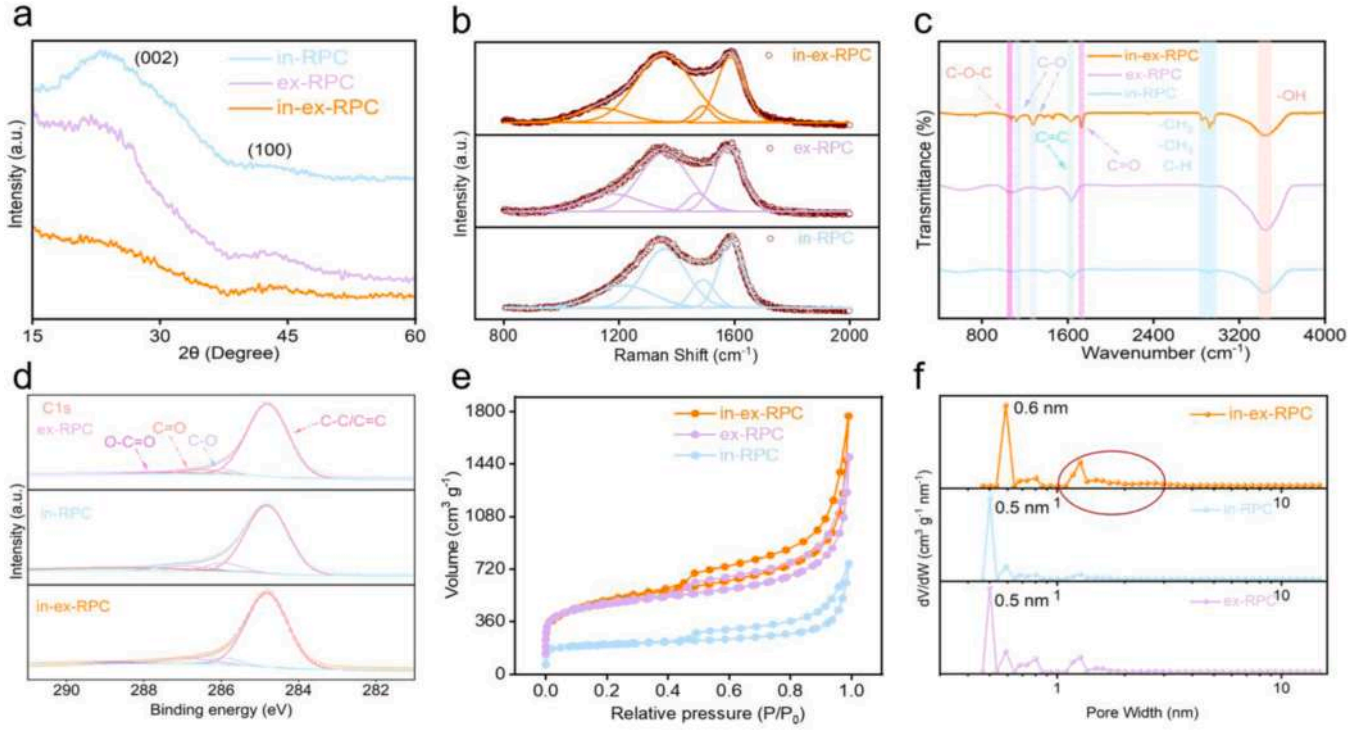

Fig. 3. Physical characteristics of in-ex-RPC, in-RPC and ex-RPC. (a) XRD patterns, (b) Raman spectra and (c) Fourier transform infrared spectra of in-ex-RPC, in-RPC and ex-RPC. (d) XPS C_{1S} spectra. (e) The isothermal nitrogen gas adsorption/desorption curves. (f) Pore size distribution plots.

Table 1
The atomic ratio of as-prepared samples through XPS analysis.

samples	C (At%)	O (At%)
in-ex-RPC	93.3%	6.7%
in-RPC	93.7%	6.3%
ex-RPC	95.1%	4.9%

Table 2
Specific surface area and pore size analysis with in-ex-RPC, in-RPC and ex-RPC. **micro**: micropores $\boldsymbol{V_{total}}$: total pore volume $\boldsymbol{V_{micro}}$: micropores volume ***APD***: average pore diameter.

Samples	S_{BET} (m^2 g^{-1})	S_{micro} (m^2 g^{-1})	S_{micro}/S_{BET} (%)	V_{total} (cm^3 g^{-1})	V_{micro} (cm^3 g^{-1})	V_{micro}/V_{total} (%)	*APD* (nm)
in-ex-RPC	1656	1095	66.1	2.74	0.77	28	6.48
in-RPC	635	431	67.8	0.97	0.31	32	7.21
ex-RPC	1546	1099	71.1	1.93	0.74	38	5.59

attached to carbon substrate surface due to re-added KOH [38], corresponding to FTIR result.

As shown in Fig. 3e and S5, the nitrogen gas adsorption-desorption isotherms of commercial activated carbon (AC), in-RPC, ex-RPC and in-ex-RPC are performed typical type-IV adsorption. At low relative pressures ($P/P_0<0.01$), the samples produce strong nitrogen gas adsorption, corresponding to existing massive micropores, while at middle-to-high relative pressure ($0.4<P/P_0<0.9$), the observed hysteresis loop represents their excellent mesoporous characteristics [42]. Correspondingly, the specific surface area, total pore volume of in-ex-RPC are 1656 m^2 g^{-1} and 2.74 cm^3 g^{-1}, which are higher than those of in-RPC (635 m^2 g^{-1}, 0.97 cm^3 g^{-1}), ex-RPC (1546 m^2 g^{-1}, 1.93 cm^3 g^{-1}), and AC (1437 m^2 g^{-1}, 0.84 cm^3 g^{-1}). Meanwhile, the average pore diameter of synthesized in-ex-RPC is 6.48 nm, which is larger than activated carbon (2.37 nm) and ex-RPC (5.59 nm) and a little smaller than in-RPC (7.21 nm) (Tables 2 and S3). Furthermore, in-ex-RPC's $S_{micro}/S_{BET} \approx 66.1\%$ deduces its specific surface area of mesopores and macropores by 33.9%, while its $V_{micro}/V_{total} \approx 28\%$ infers the pore volume proportions of mesopores and macropores by 72%, which is superior to the other three samples (in-RPC with 68%, ex-RPC with 62% and AC with 15%). Further, Fig. 3f presents the pore size distribution curves. And compared with in-RPC and ex-RPC, the 1 nm-within pores for in-ex-RPC extend to the larger region (from 0.5 nm to 0.6 nm) and the pores between 1.1–3 nm dramatically increase. Therefore, it could indicate that in-ex-RPC acquires a reasonable pore distribution by pre-embedded KOH and re-added KOH activation, achieving excellent charge storage capability and rapidly-transferring ability when applied in supercapacitors. Evidently, the three-dimensional hierarchical ramie porous carbon by internally-externally molecules-scissored activation are promising for supercapacitors, as micropores are beneficial for charges/ions storage, and mesopores are favorable for charges/ions diffusion, while macropores serve as charges/ions buffering reservoirs [43].

To give deeper expression to the electrochemical advantages of in-ex-RPC electrode materials, we compared with other in-RPC electrode materials, ex-RPC electrode materials and commercial activated carbon electrode materials. As shown in Fig. 4a and S6, the electrochemical performances of as-prepared in-ex-RPC electrode material in a three-electrode configuration with 6 M KOH aqueous electrolyte displays a specific capacitance of up to 300 F g^{-1}, which is much better than that of in-RPC (194 F g^{-1}), ex-RPC (213 F g^{-1}) or AC (139 F g^{-1}). In Fig. 4, the bulk resistance (R_s) and charge transfer resistance (R_{ct}) of the in-ex-RPC (0.67 Ω and 0.56 Ω), in-RPC (0.86 Ω and 0.21 Ω), ex-RPC (0.64 Ω and 0.66 Ω) and AC (0.81 Ω and 0.26 Ω) are small and on the same order of magnitude, presenting the low voltage drop. From Fig. 4c-d, the cyclic voltammetry curves (CV) of four electrode materials are exhibited for presenting an electric double layer capacitance [44]. Among them, the capacitance of in-ex-RPC electrode material is larger than other three electrode materials. Obviously, its galvanostatic charge/discharge curve (GCD) can more sufficiently confirm to be well consistent with the result

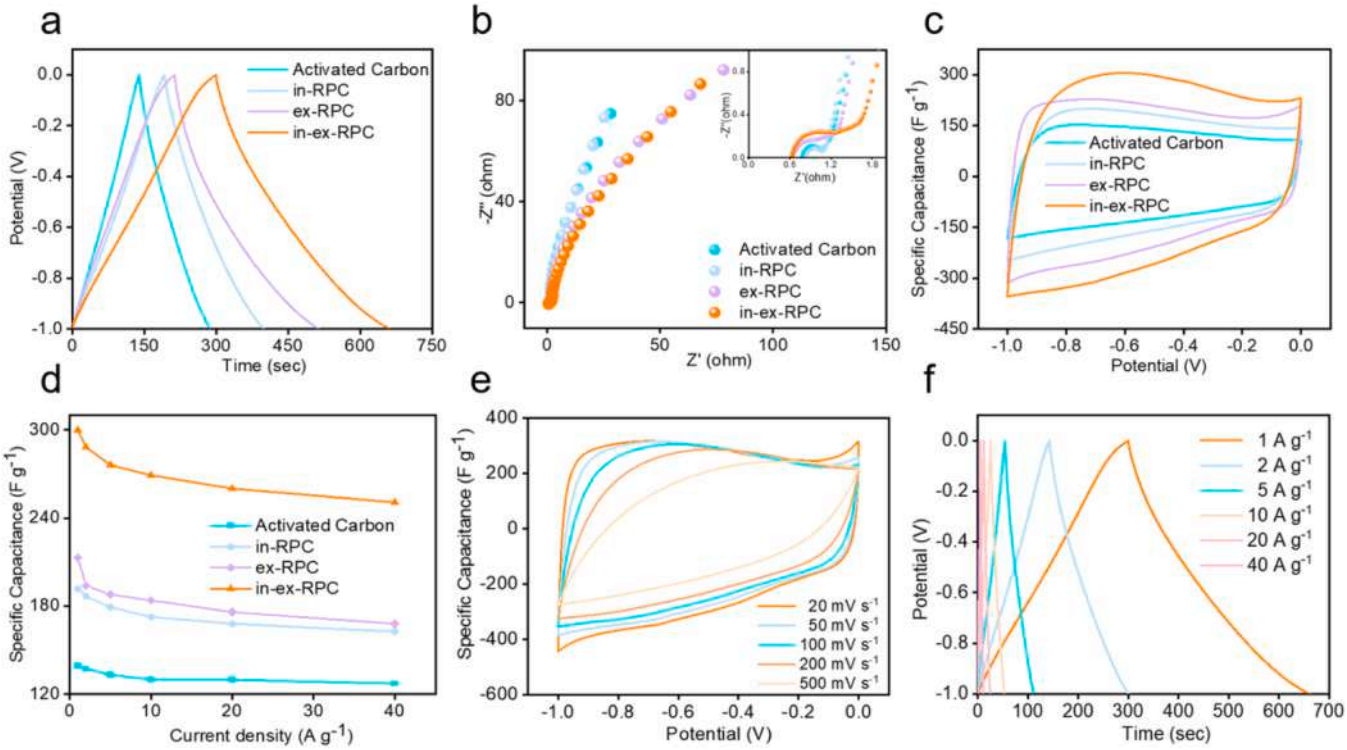

Fig. 4. Electrochemical performances of commercial activated carbon, in-ex-RPC, in-RPC and ex-RPC. (a) Galvanostatic charge/discharge curves at the current densities of 1 A g^{-1}. (b) Nyquist plots. (c) Cyclic voltammetry curves at the scan rate of 50 mV s^{-1}. (d) Rate performance of the four samples at different current densities from 1 to 40 A g^{-1}. (e) Cyclic voltammetry curves at the different scan rates of 20–500 mV s^{-1} from in-ex-RPC. (f) Galvanostatic charge/discharge curves at the different current densities of 1–40 A g^{-1} from in-ex-RPC.

of the cyclic voltammetry curve. Further, the in-ex-RPC electrode material maintains a rectangular shape at a scan rate of 500 mV s^{-1} (Fig. 4e), and even retain a specific capacitance of 251 F g^{-1} when the current density is increased by 40 times (40 A g^{-1}), performing excellent rate capability with 83.6% (Fig. 4f).

Fig. 5a schematically shows the charge or discharge circuit of symmetric supercapacitors with 6 M aqueous KOH electrolyte. As a result, all the galvanostatic charge/discharge curves exhibit similar with isosceles triangle and the specific capacitance of in-ex-RPC is up to 65.7 F g^{-1} at the current density of 1 A g^{-1}, which exceeds those of in-RPC, ex-RPC and commercial activated carbon based aqueous symmetric supercapacitors (36.2 F g^{-1}, 46.3 F g^{-1} and 30 F g^{-1}). Even at 40 A g^{-1}, it can still maintain a specific capacitance of 56.3 F g^{-1}, suggesting exceptional rate capability of 85.7%. And all the cyclic voltammetry curves display rectangular shape, which authenticates the double layer capacitance behavior (Fig. 5b, c, d and g). Also, the R_s and R_{ct} of in-ex-RPC (0.4 Ω and 0.26 Ω), in-RPC (0.33 Ω and 0.21 Ω), ex-RPC (0.6 Ω and 0.4 Ω) and AC (0.34 Ω and 0.12 Ω) present low resistance and further indicate low voltage drop when charging and discharging (Fig. 5e and S7). It should be noted that the cyclic voltammetry of in-ex-RPC based aqueous symmetric supercapacitors could retain an approximately good rectangular shape at a high scan rate of 2000 mV s^{-1} (Fig. 5f). Besides, the Ragone plots of in-ex-RPC based aqueous symmetric supercapacitors deliver a high energy density of 9.125 W h kg^{-1} at power density of 0.5 KW kg^{-1}. Even at a high power density of 20 KW kg^{-1}, it can still retain a high energy density of 7.81 W h kg^{-1}, which are larger than those of the previously-reported carbon materials (Fig. 5h) [45–48]. At the current density of 5 A g^{-1}, its cyclic capacity retains 90.9% of its initial capacity after 20,000 cycles, which is higher than that of in-RPC (89.6%), but a little lower than those of activated carbon (93.8%) and ex-RPC (91.6%). (Fig. 5i and S8). What's more, From Fig. 5j, all the integrational series and parallel aqueous symmetric devices performs good rectangular shape, indicating excellent electric double layer capacitance characteristic. Meanwhile in Fig. S9 the series devices were used for set a timer, which keeps it on for about four minutes.

To improve the working voltage and further to obtain a higher energy density, we developed the in-ex-RPC based symmetric supercapacitors with $EMIMBF_4$ ionic liquid electrolyte. As shown in Fig. 6a-, the GCD curves perform that the specific capacitance is 38.5 F g^{-1} at 1 A g^{-1} and maintain 71.2% of initial capacity at 40 A g^{-1}. From Fig. 6c, this supercapacitor can deliver a working window of 3.5 V and retain rectangular CV shape at a high scan rate of 1000 mV s^{-1}. Meanwhile, the Electrochemical Impedance Spectroscopy analysis could comprehend the resistance behavior in $EMIMBF_4$ ionic liquid electrolyte. Although ionic liquids can provide the advantage of higher working voltage, their ionic conductivities are generally one order of magnitude lower than that of the aqueous electrolytes, resulting in higher resistance [49]. Not surprisingly, the R_s (2.9 Ω) and R_{ct} (1.1 Ω) are both larger than those in 6 M KOH electrolyte (0.4 Ω and 0.26 Ω) (Fig. 6d). In addition, the Ragone plots deliver a high energy density of 65.5 W h kg^{-1} at power density of 1.76 KW kg^{-1} and retain 46.6 W h kg^{-1} at a high power density of 91.6 KW kg^{-1} (Fig. 6e). Furthermore, as shown in Fig. 6f, both the series and parallel devices perform rectangular CV shape at 50 mV s^{-1} compared with the single device, which reveals a valuable integration application.

The whole excellent electrochemical performances of symmetric supercapacitors with aqueous KOH and $EMIMBF_4$ electrolytes are attributed to waste ramie straw and simplified synergistic activation process. First, the low-cost, environmentally-friendly, massively three-harvests-one-year and naturally channel-structured ramie straw could be conductive for the ionic transmission for energy storage, while hierarchically interconnected three-dimensional porous carbon from waste ramie straw possesses high specific surface area of up to 1656 m^2 g^{-1}, reasonable pore distribution (V_{total} = 2.74 cm^3 g^{-1}) and average pore diameter of 6.48 nm, efficiently guaranteeing the superior capacitance, rate capability, cyclic stability, power density and energy density of

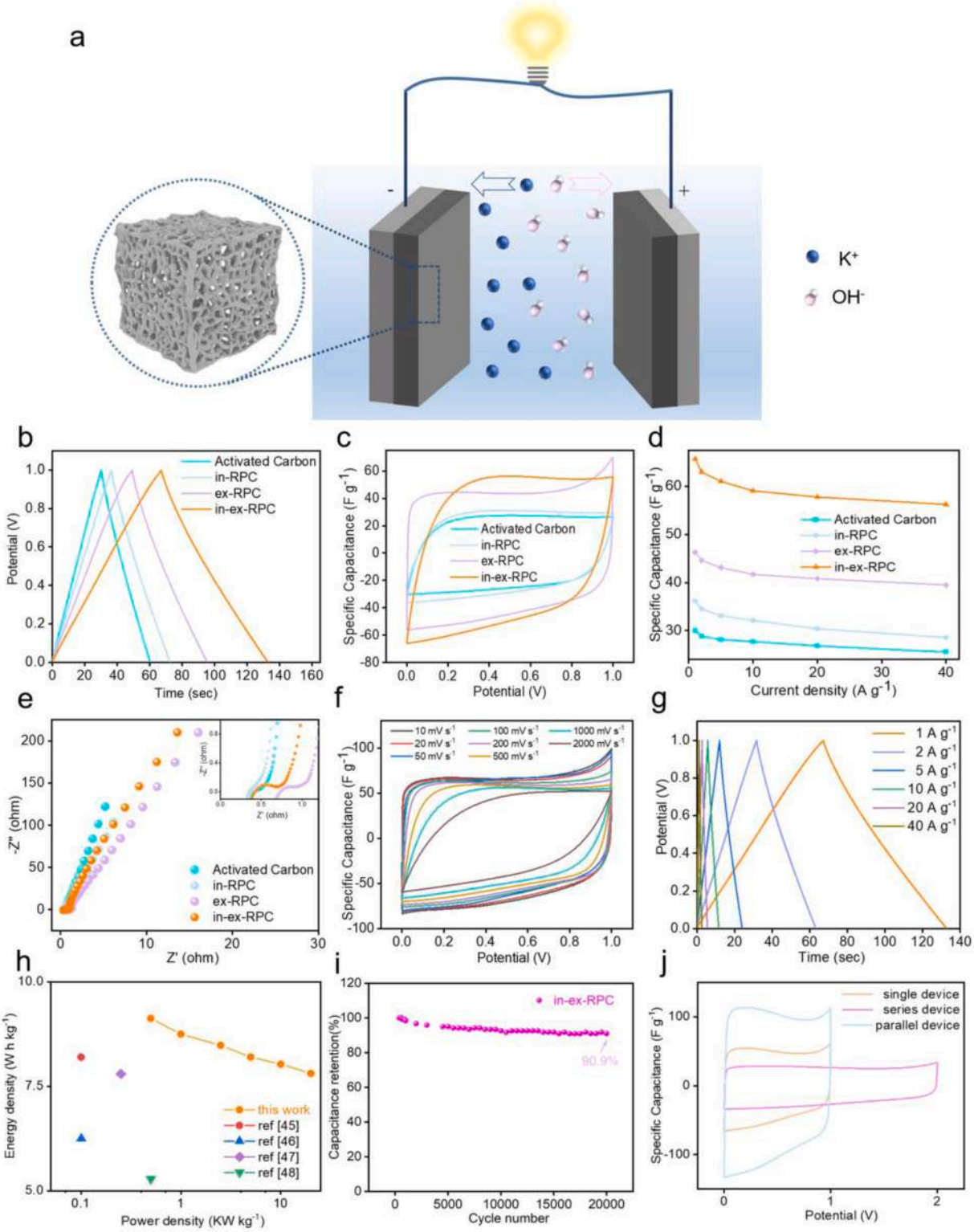

Fig. 5. Electrochemical performances of commercial activated carbon, in-ex-RPC, in-RPC, and ex-RPC based symmetric supercapacitors with 6 M KOH electrolyte. (a) Schematic diagram of symmetric supercapacitors with 6 M KOH electrolyte. (b) Galvanostatic charge/discharge curves at the current density of 1 A g^{-1}. (c) Cyclic voltammetry curves at the scan rate of 50 mV s^{-1}. (d) Rate performances of the four supercapacitors at different current densities from 1 to 40 A g^{-1}. (e) Nyquist plots. (f) Cyclic voltammetry curves at the different scan rates of 10–2000 mV s^{-1} from in-ex-RPC based symmetric supercapacitors. (g) Galvanostatic charge/discharge curves at the different current densities of 1–40 A g^{-1} from in-ex-RPC based symmetric supercapacitors. (h) Ragone plots of the power density and energy density of in-ex-RPC based symmetric supercapacitors in comparison to other carbon materials. (i) Cycling performance of in-ex-RPC based symmetric supercapacitors with 6 M KOH electrolyte within 20,000 cycles at the current density of 5 A g^{-1}. (j) The single and two-unit symmetric supercapacitors with 6 M KOH electrolyte in series and parallel.

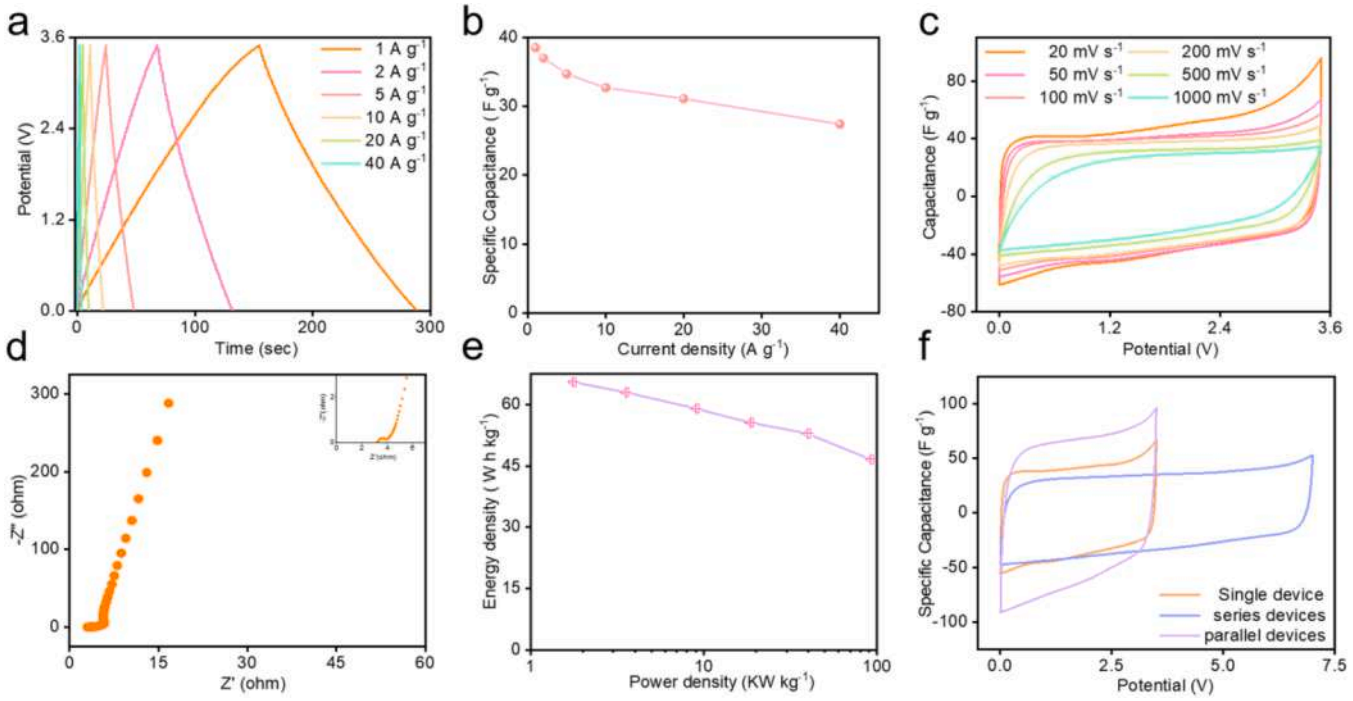

Fig. 6. Electrochemical performances of in-ex-RPC based symmetric supercapacitors with $EMIMBF_4$ ionic liquid electrolyte. (a) Galvanostatic charge/discharge curves at the different current densities of 1–40 A g^{-1}. (b) Rate performance of the supercapacitors at different current densities from 1 to 40 A g^{-1}. (c) Cyclic voltammetry curves at the different scan rates of 20–1000 mV s^{-1}. (d) Nyquist plot. (e) Ragone plots of the power density and energy density with $EMIMBF_4$ ionic liquid electrolyte. (f) Cyclic voltammetry curves at a scan rate of 50 mV s^{-1} from the single device, two series and parallel devices.

symmetric supercapacitors. What's more, this operational synergistic activation process dramatically expands massive production and commercial applications of ramie porous carbon, and it is worth remarkable to recycle the waste ramie straw to decrease natural resources waste and environmental pollution, even broaden its application field. Last but not least, compared to onion carbon, graphene and carbon nanotube, the high-specific-surface-area and reasonable-pore-distribution ramie porous carbon has been expected to be broadly used in single or integrated multilayer soft roll and cylindrical-shaped supercapacitors for high power output and further industrialization.

4. Conclusion

In conclusion, we demonstrated a hierarchically interconnected three-dimensional porous carbon prepared through ramie straw based around the internally-externally molecules-scissored activation with pre-embedded KOH and re-added KOH molecules. This peculiar structure of in-ex-RPC accomplished a high specific surface area of 1656 m^2 g^{-1}, pore volume of 2.74 cm^3 g^{-1} and average pore diameter of 6.48 nm. Furthermore, the in-ex-RPC electrode material displays a specific capacitance of 300 F g^{-1}. Based on it, the aqueous 6 M KOH based symmetric supercapacitors deliver a high power density of 0.5 KW kg^{-1}, a high energy density of 9.125 W h kg^{-1} and a cyclic capacity of 90.9%-retaining after 20,000 cycles at 5 A g^{-1}. Simultaneously, the 1-ethyl-3-methyl imidazolium tetrafluoroborate salt ($EMIMBF_4$) ionic liquid electrolyte based symmetric supercapacitors supply a high energy density of 65.5 W h kg^{-1} at a high power density of 1.76 KW kg^{-1}. These accessible consequences indicate that the hierarchically interconnected three-dimensional structures can provide an extremely effective strategy to promote energy density of ramie carbon and broaden the applications in impurities adsorption and catalysis.

Data availability

The data that support the findings of this study are available within the article and its supplementary material.

CRediT authorship contribution statement

Yuyang Chen: Formal analysis, Conceptualization, Investigation, Methodology, Visualization, Writing – original draft. **Qing Wang:** Investigation, Methodology. **Ningjun Chen:** Investigation. **Qitian Luo:** Investigation. **Haijian Li:** Investigation. **Jie Li:** Investigation. **Weiqing Yang:** Funding acquisition, Supervision, Writing – review & editing.

Declaration of Competing Interest

The authors declare that they have no known competing financial interests or personal relationships that could have appeared to influence the work reported in this paper.

Data Availability

Data will be made available on request.

Acknowledgements

This work is supported by the National Natural Science Foundation of China (No. 51977185 and No. 51972277) and the Sichuan Science and Technology Program (No. 2018RZ0074). We are also gratitude to the Analytical and Testing Center of Southwest Jiaotong University for providing the characteristic measurements.

Supplementary materials

Supplementary material associated with this article can be found, in the online version, at doi:10.1016/j.electacta.2022.141583.

References

[1] A.G. Olabi, Renewable energy and energy storage systems, Energy 136 (2017) 1–6.
[2] Q. Jiang, Z. Zhang, S. Yin, Z. Guo, S. Wang, C. Feng, Biomass carbon micro/nano-structures derived from ramie fibers and corncobs as anode materials for lithium-ion and sodium-ion batteries, Appl. Surf. Sci. 379 (2016) 73–82.
[3] C. Jin, J. Nai, O. Sheng, H. Yuan, W. Zhang, X. Tao, X.W. Lou, Biomass-based materials for green lithium secondary batteries, Energy Environ. Sci. 14 (3) (2021) 1326–1379.
[4] W. Long, B. Fang, A. Ignaszak, Z. Wu, Y.J. Wang, D. Wilkinson, Biomass-derived nanostructured carbons and their composites as anode materials for lithium ion batteries, Chem. Soc. Rev. 46 (23) (2017) 7176–7190.
[5] J. Niu, R. Shao, J. Liang, M. Dou, Z. Li, Y. Huang, F. Wang, Biomass-derived mesopore-dominant porous carbons with large specific surface area and high defect density as high performance electrode materials for Li-ion batteries and supercapacitors, Nano Energy 36 (2017) 322–330.
[6] K. Yu, Z. Zhang, J. Liang, C. Liang, Natural biomass-derived porous carbons from buckwheat hulls used as anode for lithium-ion batteries, Diam. Relat. Mater. 119 (2021), 108533.
[7] Y.-.C. Zhang, Y. You, S. Xin, Y.-.X. Yin, J. Zhang, P. Wang, X.-s. Zheng, F.-.F. Cao, Y.-.G. Guo, Rice husk-derived hierarchical silicon/nitrogen-doped carbon/carbon nanotube spheres as low-cost and high-capacity anodes for lithium-ion batteries, Nano Energy 25 (2016) 120–127.
[8] D. Liu, Q. Li, J. Hou, H. Zhao, Porous 3D graphene-based biochar materials with high areal sulfur loading for lithium–sulfur batteries, Sustain. Energy Fuels 2 (10) (2018) 2197–2205.
[9] Y. Qu, Z. Zhang, X. Zhang, G. Ren, Y. Lai, Y. Liu, J. Li, Highly ordered nitrogen-rich mesoporous carbon derived from biomass waste for high-performance lithium–sulfur batteries, Carbon NY 84 (2015) 399–408.
[10] W. Wang, Y. Zhao, Y. Zhang, N. Liu, Z. Bakenov, Nickel embedded porous macrocellular carbon derived from popcorn as sulfur host for high-performance lithium-sulfur batteries, J. Mater. Sci. Technol. 74 (2021) 69–77.
[11] L. Zhu, H. Jiang, W. Ran, L. You, S. Yao, X. Shen, F. Tu, Turning biomass waste to a valuable nitrogen and boron dual-doped carbon aerogel for high performance lithium-sulfur batteries, Appl. Surf. Sci. 489 (2019) 154–164.
[12] A. Khan, R.A. Senthil, J. Pan, S. Osman, Y. Sun, X. Shu, A new biomass derived rod-like porous carbon from tea-waste as inexpensive and sustainable energy material for advanced supercapacitor application, Electrochimi. Acta 335 (2020), 135588.
[13] X. Liang, R. Liu, X. Wu, Biomass waste derived functionalized hierarchical porous carbon with high gravimetric and volumetric capacitances for supercapacitors, Microporous Mesoporous Mater. 310 (2021), 110659.
[14] M. Song, Y. Zhou, X. Ren, J. Wan, Y. Du, G. Wu, F. Ma, Biowaste-based porous carbon for supercapacitor: the influence of preparation processes on structure and performance, J. Colloid Interface Sci. 535 (2019) 276–286.
[15] L. Sun, C. Tian, M. Li, X. Meng, L. Wang, R. Wang, J. Yin, H. Fu, From coconut shell to porous graphene-like nanosheets for high-power supercapacitors, J. Mater. Chem. A 1 (21) (2013) 6462–6470.
[16] W. Zhang, B. Liu, M. Yang, Y. Liu, H. Li, P. Liu, Biowaste derived porous carbon sponge for high performance supercapacitors, J. Mater. Sci. Technol. 95 (2021) 105–113.
[17] F. Liu, Z. Wang, H. Zhang, L. Jin, X. Chu, B. Gu, H. Huang, W. Yang, Nitrogen, oxygen and sulfur co-doped hierarchical porous carbons toward high-performance supercapacitors by direct pyrolysis of kraft lignin, Carbon NY 149 (2019) 105–116.
[18] Q. Wang, Y. Chen, X. Jiang, X. Qiao, Y. Wang, H. Zhao, B. Pu, W. Yang, Self-assembly defect-regulating superstructured carbon, Energy Storage Mater. 48 (2022) 164–171.
[19] Q. Wang, F. Liu, Z. Jin, X. Qiao, H. Huang, X. Chu, D. Xiong, H. Zhang, Y. Liu, W. Yang, Hierarchically divacancy defect building dual-activated porous carbon fibers for high-performance energy-storage devices, Adv. Funct. Mater. 30 (39) (2020), 2002580.
[20] Q. Wang, Y. Zhou, X. Zhao, K. Chen, G. Bingni, T. Yang, H. Zhang, W. Yang, J. Chen, Tailoring carbon nanomaterials via a molecular scissor, Nano Today 36 (2021), 101033.
[21] W. Ao, J. Fu, X. Mao, Q. Kang, C. Ran, Y. Liu, H. Zhang, Z. Gao, J. Li, G. Liu, J. Dai, Microwave assisted preparation of activated carbon from biomass: a review, Renew. Sust. Energ. Rev. 92 (2018) 958–979.
[22] F. Wang, F. Zheng, J. Jiang, Y. Li, Y. Luo, K. Chen, J. Du, Y. Huang, Q. Li, H. Wang, Microwave-assisted preparation of hierarchical N and O Co-doped corn-Cob-derived activated carbon for a high-performance supercapacitor, Energy Fuels 35 (9) (2021) 8334–8344.
[23] W.H. Qu, Y.Y. Xu, A.H. Lu, X.Q. Zhang, W.C. Li, Converting biowaste corncob residue into high value added porous carbon for supercapacitor electrodes, Bioresour. Technol. 189 (2015) 285–291.
[24] S. Wang, W. Sun, D.-.S. Yang, F. Yang, Conversion of soybean waste to sub-micron porous-hollow carbon spheres for supercapacitor via a reagent and template-free route, Mater. Today Energy 13 (2019) 50–55.
[25] Y. Ding, Y. Li, Y. Dai, X. Han, B. Xing, L. Zhu, K. Qiu, S. Wang, A novel approach for preparing in-situ nitrogen doped carbon via pyrolysis of bean pulp for supercapacitors, Energy 216 (2021), 119227.
[26] S.S. Gunasekaran, S. Badhulika, High-performance solid-state supercapacitor based on sustainable synthesis of meso-macro porous carbon derived from hemp fibres via CO_2 activation, J. Energy Storage 41 (2021), 102997.
[27] M. Yu, Y. Han, J. Li, L. Wang, CO_2 -activated porous carbon derived from cattail biomass for removal of malachite green dye and application as supercapacitors, Chem. Eng. J. 317 (2017) 493–502.
[28] C. Chen, D. Yu, G. Zhao, B. Du, W. Tang, L. Sun, Y. Sun, F. Besenbacher, M. Yu, Three-dimensional scaffolding framework of porous carbon nanosheets derived from plant wastes for high-performance supercapacitors, Nano Energy 27 (2016) 377–389.
[29] L. Guan, L. Pan, T. Peng, C. Gao, W. Zhao, Z. Yang, H. Hu, M. Wu, Synthesis of Biomass-Derived Nitrogen-Doped Porous Carbon Nanosheests for High-Performance Supercapacitors, ACS Sustain. Chem. Eng. 7(9) (2019) 8405–8412.
[30] S. Lu, W. Yang, M. Zhou, L. Qiu, B. Tao, Q. Zhao, X. Wang, L. Zhang, Q. Xie, Y. Ruan, Nitrogen- and oxygen-doped carbon with abundant micropores derived from biomass waste for all-solid-state flexible supercapacitors, J. Colloid Interface Sci. 610 (2022) 1088–1099.
[31] A.R. Selvaraj, A. Muthusamy, C. Inho, H.-.J. Kim, K. Senthil, K. Prabakar, Ultrahigh surface area biomass derived 3D hierarchical porous carbon nanosheet electrodes for high energy density supercapacitors, Carbon NY 174 (2021) 463–474.
[32] A.A. Mohammed, C. Chen, Z. Zhu, Low-cost, high-performance supercapacitor based on activated carbon electrode materials derived from baobab fruit shells, J. Colloid Interface Sci. 538 (2019) 308–319.
[33] P. Ozpinar, C. Dogan, H. Demiral, U. Morali, S. Erol, C. Samdan, D. Yildiz, I. Demiral, Activated carbons prepared from hazelnut shell waste by phosphoric acid activation for supercapacitor electrode applications and comprehensive electrochemical analysis, Renew. Energ. 189 (2022) 535–548.
[34] G. Ma, Q. Yang, K. Sun, H. Peng, F. Ran, X. Zhao, Z. Lei, Nitrogen-doped porous carbon derived from biomass waste for high-performance supercapacitor, Bioresour. Technol. 197 (2015) 137–142.
[35] L. Li, C. Jia, X. Zhu, S. Zhang, Utilization of cigarette butt waste as functional carbon precursor for supercapacitors and adsorbents, J. Clean. Prod. 256 (2020), 120326.
[36] D. Tang, Y. Luo, W. Lei, Q. Xiang, W. Ren, W. Song, K. Chen, J. Sun, Hierarchical porous carbon materials derived from waste lentinus edodes by a hybrid hydrothermal and molten salt process for supercapacitor applications, Appl. Surf. Sci. 462 (2018) 862–871.
[37] J. Yang, J. Meng, Y. Zhu, Q. Liu, X. Zhang, X. Zheng, Superior capacitive performance of micropore-dominant porous carbon derived from biomass wastes, J. Energy Storage 50 (2022), 104668.
[38] M. Li, C. Liu, H. Cao, H. Zhao, Y. Zhang, Z. Fan, KOH self-templating synthesis of three-dimensional hierarchical porous carbon materials for high performance supercapacitors, J. Mater. Chem. A 2 (36) (2014) 14844–14851.
[39] F. Yang, S. Zhang, H. Li, S. Li, K. Cheng, J.-.S. Li, D.C.W. Tsang, Corn straw-derived biochar impregnated with α-FeOOH nanorods for highly effective copper removal, Chem. Eng. J. 348 (2018) 191–201.
[40] M. Varga, T. Izak, V. Vretenar, H. Kozak, J. Holovsky, A. Artemenko, M. Hulman, V. Skakalova, D.S. Lee, A. Kromka, Diamond/carbon nanotube composites: raman, FTIR and XPS spectroscopic studies, Carbon NY 111 (2017) 54–61.
[41] X. Xiao, B. Chen, L. Zhu, Transformation, morphology, and dissolution of silicon and carbon in rice straw-derived biochars under different pyrolytic temperatures, Environ. Sci. Technol. 48 (6) (2014) 3411–3419.
[42] R. Bardestani, G.S. Patience, S. Kaliaguine, Experimental methods in chemical engineering: specific surface area and pore size distribution measurements—BET, BJH, and DFT, Can. J. Chem. Eng. 97 (11) (2019) 2781–2791.
[43] L. Qie, W. Chen, H. Xu, X. Xiong, Y. Jiang, F. Zou, X. Hu, Y. Xin, Z. Zhang, Y. Huang, Synthesis of functionalized 3D hierarchical porous carbon for high-performance supercapacitors, Energy Environ. Sci. 6 (8) (2013) 2497–2504.
[44] N.S. Choi, Z. Chen, S.A. Freunberger, X. Ji, Y.K. Sun, K. Amine, G. Yushin, L. F. Nazar, J. Cho, P.G. Bruce, Challenges facing lithium batteries and electrical double-layer capacitors, Angew. Chem. Int. Ed. Engl. 51 (40) (2012) 9994–10024.
[45] P. Cheng, S. Gao, P. Zang, X. Yang, Y. Bai, H. Xu, Z. Liu, Z. Lei, Hierarchically porous carbon by activation of shiitake mushroom for capacitive energy storage, Carbon NY 93 (2015) 315–324.
[46] H. Feng, H. Hu, H. Dong, Y. Xiao, Y. Cai, B. Lei, Y. Liu, M. Zheng, Hierarchical structured carbon derived from bagasse wastes: a simple and efficient synthesis route and its improved electrochemical properties for high-performance supercapacitors, J. Power Sources 302 (2016) 164–173.
[47] Y. Huang, L. Peng, Y. Liu, G. Zhao, J.Y. Chen, G. Yu, Biobased nano porous active carbon fibers for high-performance supercapacitors, ACS Appl. Mater. Interfaces 8 (24) (2016) 15205–15215.
[48] M. Zhong, H. Liu, M. Wang, Y.W. Zhu, X.Y. Chen, Z.J. Zhang, Hierarchically N/O-enriched nanoporous carbon for supercapacitor application: simply adjusting the composition of deep eutectic solvent as well as the ratio with phenol-formaldehyde resin, J. Power Sources 438 (2019), 226982.
[49] C. Zhong, Y. Deng, W. Hu, J. Qiao, L. Zhang, J. Zhang, A review of electrolyte materials and compositions for electrochemical supercapacitors, Chem. Soc. Rev. 44 (21) (2015) 7484–7539.